

Computational study of flowfield characteristics in cavities with stores

B. Khanal*, K. Knowles[†] and A. J. Saddington[‡]

Cranfield University

Defence Academy of the United Kingdom

Shrivenham, SN6 8LA, England

Abstract

In this paper, the results of computational studies on the unsteady flow features in three-dimensional empty cavities and cavities with a representative store are presented. Flow simulations with a turbulence model based on a hybrid method, which behaves as a standard Reynolds-averaged Navier-Stokes (RANS) model within the attached boundary layer and as a Large-Eddy Simulation LES Sub-Grid Scale model in the rest of the flow (commonly known as Detached-Eddy Simulation [DES]) are used in this study. The time-mean flow study showed the presence of three-dimensional effects inside the cavities. The mean flowfield visualisation also clearly showed the presence of a pair of 'tornado-like' vortices in the upstream half of the cavity which merge to a single, large recirculation further downstream. Visualisation for the cavity-with-store case revealed that the mean flowfield was effectively divided into two halves with significant reduction of the spanwise flow across the cavity width. In the unsteady flow study, near-field acoustic spectra were computed for the empty cavity and cavity-with-store cases. Study of unsteady pressure spectra for the cavity-with-store case found the presence of many peaks and the corresponding mode frequencies were found to agree well with the Rossiter modes. The blockage effect of store and strut on the spanwise flow is thought to have reduced the interaction, and subsequent non-linear coupling, between the Rossiter modes. This may be the reason for the co-existence of multiple modes without the coupling among them.

*Research Student; Aeromechanical Systems Group

[†]Professor and Head of Aeromechanical Systems Group

[‡]Lecturer; Aeromechanical Systems Group

Nomenclature

2D	Two-dimensional
3D	Three-dimensional
CFD	Computational fluid dynamics
C_p	Pressure Coefficient
D	Cavity depth, m
f_n	frequency of the n^{th} mode, Hz
K	ratio of the velocity in the shear layer to the freestream velocity
L	Cavity length, m
LIC	Line Integral Convolution
M_∞	Flow Mach number
n	Cavity oscillation mode number
St	Strouhal number, $St = fD/U_\infty$
U_∞	Freestream velocity, m/s
W	Cavity width, m
x, y, z	Cartesian coordinate system, origin at the top left corner of the upstream wall
α	an empirical constant, $\alpha = 0.062(L/D)$
δ	Boundary layer thickness at a velocity of $0.99U_\infty$, m
ρ	fluid density, kg/m ³
γ	Ratio of specific heats of test fluid ($\gamma = 1.4$ for air)

1 Introduction

From simple surface cutouts to more complicated shapes with internal structures, cavity flowfields are widely present in many aerospace applications, such as wheel wells, weapons bays, and other fuselage openings and are also well-documented as aerodynamic noise sources. Unsteady flow approaching a simple cavity geometry produces complex features consisting of flow-induced resonant tones, multiple flow and acoustic instabilities, and wave interactions. Internal weapons bays on military aircraft, in particular, have several design advantages. Reduced aerodynamic drag, low radar cross-section and avoidance of aerodynamic heating of the store are a few examples of these. However, once the weapons bay doors are opened, the flowfield is dependent on the cavity geometry and the freestream flow conditions. The resultant unsteady

flowfield undergoes interaction with the stores at the beginning of the store release leading to several undesirable aerodynamic effects. Firstly, the self-sustaining pressure fluctuations in the cavity cause cavity resonance which in turn leads to structural fatigue of the aircraft and the store. Secondly, the interaction of the store with the unsteady shear layer formed over the cavity can lead to unpredicted motion of the store. Hence, a study of cavity flowfields is necessary to understand these phenomena.

Numerous experimental and computational research studies [1, 2, 3, 4, 5] have been carried out to understand complex flow features existing in cavities and many more are continuing to understand the cause behind such complex flowfields and to try to suppress the resonant tones. Several computational studies in the past have experienced a limitation with Reynolds-averaged Navier-Stokes (RANS) and turbulence models applied to unsteady flows [6, 7, 8]. The RANS solver produces increased eddy viscosity which causes excessive damping of the unsteadiness of the flowfield. Spatially filtered models such as Large-Eddy Simulation (LES) have provided improved results for simulating unsteady flows. LES models, however, are currently limited to low Reynolds numbers because of the computing resources required to resolve the small-scale turbulent structures. LES is not yet, therefore, a feasible tool for the simulation of cavity flowfields at transonic speeds. Recently, hybrid methods which behave as a standard RANS model within the attached boundary layer and as a LES Sub-Grid Scale model in the rest of the flow [more commonly known as Detached Eddy Simulation (DES)] have been introduced to address this problem [6, 9, 5]. Flow simulations with a turbulence model based on a one-equation DES formulation [6] are used in this study.

Cavity flows are usually classified by the length-to-depth ratio (L/D) of the cavity and four different types of cavity flows have been identified depending on the value of this ratio. Early studies based on the analysis of wake flows by Charwat *et al.* [10, 11] led to the characterisation of three distinct types of cavity flows based on the cavity floor pressure distributions which are primarily dependent on the geometry of the cavity. These were categorized as open, closed and intermediate (also known as transitional) flow. In the 1980s, Stallings and Wilcox [4] studied the cavity pressure distribution at supersonic speeds experimentally. Their work led to a more detailed classification of the flow types and the transitional flow type was further explained and divided into transitional open and transitional closed flows. Schematics representing all four cavity flow types and corresponding floor pressure distributions are shown in Figure 1.

Cavity flows exhibit a wide variety of phenomena whose precise nature depends sensitively

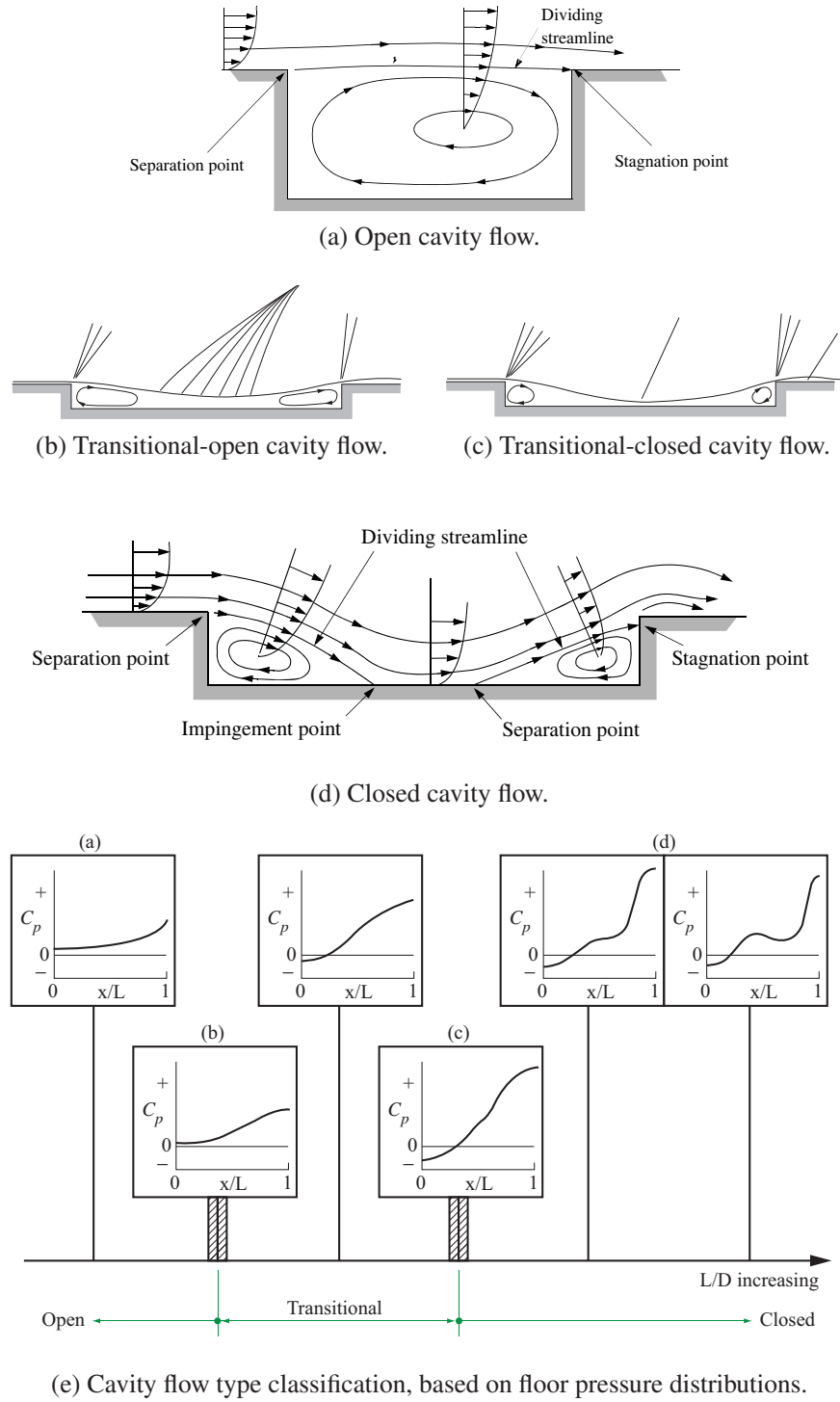


Figure 1: Cavity flow types and corresponding pressure distributions [12].

on a number of parameters including the value of L/D . In the literature, vastly different values of L/D have been quoted to define the flow types. For instance: $L/D < 7$ for open and $L/D > 13$ for closed cavity flow is reported by Stallings and Wilcox [4] whereas $L/D < 10$ for open and $L/D > 13$ for closed cavity flow is reported in the work of Plentovich [13]. Similarly, Dix and Bauer [1] quote $L/D < 9$ for open and $L/D > 13$ for closed cavity flow whereas Srinivisan and Baysal [2] quote $L/D < 3$ for open and $L/D > 10$ for closed cavity flowfields. Tracy and Plentovich [14] investigated the variations in the values of L/D and concluded that the vast disagreements in the literature were due to the dependence of the cavity flow type on Mach number as well as L/D . The other important parameters that affect cavity flow types are incoming boundary layer thickness (δ), ambient density (ρ), viscosity (μ), and speed of sound (a_0). Although the underlying physical mechanisms vary, it is known that self-sustaining oscillations develop over a wide range of these parameters. In compressible flows, cavity oscillations are typically described as a flow-acoustic resonance mechanism. This mechanism may be summarized as follows: small instabilities in the shear layer interact with the downstream edge of the cavity and generate acoustic waves. These acoustic waves propagate upstream to the region near shear layer separation where they induce localized instabilities, thereby closing the feedback loop. This type of instability is referred to as a shear-layer (or more commonly Rossiter) mode, attributed to the early experimental work of Rossiter [15]. This led to the development of a well-known semi-empirical formula which can be used to predict a given mode frequency of oscillation for a given cavity geometry:

$$f_n = \frac{U_\infty}{L} \left(\frac{n - \alpha}{M_\infty + \frac{1}{K}} \right) \quad (1)$$

where f_n is the frequency corresponding to the n^{th} mode, M_∞ is the freestream Mach number, K is the ratio of disturbance velocity in the shear layer to the freestream velocity, (a value of $K = 0.57$ is widely used; although this value is appropriate for thin initial boundary layers, it decreases with increasing boundary layer thickness) and α is an empirical constant employed to account for the phase lag between the passage of a vortical disturbance past the cavity trailing edge and the formation of an upstream travelling disturbance. The value of α depends on L/D and is evaluated as : $\alpha = 0.062(L/D)$. Rossiter's model is generally found to agree well with experimental results at moderate subsonic Mach numbers. At transonic and supersonic Mach

numbers temperature recovery within the cavity is important and hence it is essential to account for the increased sound speed within the cavity [16]. To accommodate these high Mach number ranges, Eq. 1 was subsequently modified to predict the frequencies of the various oscillation modes as follows:

$$f_n = \frac{U_\infty}{L} \left(\frac{n - \alpha}{M_\infty \left[1 + \frac{(\gamma-1)}{2} M_\infty^2 \right]^{-\frac{1}{2}} + \frac{1}{K}} \right) \quad (2)$$

where γ is the ratio of specific heats of the test fluid ($\gamma = 1.4$ for air).

In this paper results from the computational investigations of open cavity flows are presented. Eq. 2, also known as the "modified Rossiter Equation", is used here to predict the frequencies of the various oscillation modes in cavities for comparison with the computed results. This work is a continuation of our effort [17] on understanding the cavity flowfield behaviours in the presence of a store in the cavity.

2 Computational Solver

The commercial CFD solver FLUENT was used to simulate all the cavity cases considered in this paper. FLUENT is a finite-volume solver and the temporal and spatial discretization schemes available in it provide at most second-order accuracy in space and time. Many studies [18, 19] have shown FLUENT to be capable of simulating unsteady flow problems, and of resolving the flow structures responsible for noise generation when suitably designed computational mesh and time-step sizes are used. Options for both explicit as well as the implicit time-stepping are available with the solver. The implicit time-stepping option was used on all the simulated results presented in this paper. To model the turbulent unsteady flowfield inside the cavity, Detached-Eddy Simulation (DES) based on a one-equation model [20] was used. DES is a hybrid model which behaves as a standard SA RANS model within the attached boundary layer and as a Large-Eddy Simulation (LES) Sub-Grid Scale (SGS) model in the rest of the flow. The standard RANS SA turbulence model [20] uses the distance to the nearest wall to define a length scale d that is used to calculate the production and the dissipation terms of turbulent viscosity. In the DES formulation of the SA turbulence model [6], the length scale d is replaced with a DES length scale d_{DES} defined as:

$$d_{DES} = \min(d, C_{DES}\Delta) \quad (3)$$

$$\Delta = \max(\delta x, \delta y, \delta z) \quad (4)$$

where C_{DES} is a constant with a value of 0.65 for the DES model and Δ is the largest cell dimension in the computational grid. The modified length scale calculated using the relations in Eq. 3 ensures a length scale that is the same as the standard SA RANS value near the walls where $d \ll \Delta$ and reduces to the local grid spacing away from the walls where $d \gg \Delta$. The effect of this is to activate a hybrid SA turbulence model that behaves as a standard SA RANS model within the attached boundary layers and as a LES Sub-Grid Scale model in the rest of the flow including the separated regions. From Eq. 3, it can clearly be seen that this model is grid-dependent and, hence, any solution using it also relies on the grid design, i.e. depending on whether the cells in the attached boundary layer are carefully designed, a local grid spacing as the length scale will be activated rather than the standard SA RANS length scale required in the boundary layer.

3 Boundary Conditions and Solver Settings

All the solid surfaces (cavity walls and flat plate) were treated as adiabatic walls with a no-slip condition. The rest of the boundary faces were set as pressure farfield. The spacial discretization used was flux difference splitting based on second-order upwind (default option for compressible flow in Fluent) with a second-order central differencing applied to the modified turbulent viscosity and a second-order implicit scheme adapted for temporal discretization. Due to the transonic speed involved, a coupled solver was chosen to ensure a fully compressible solution and a constant time step (constant time-stepping is essential for the time consistency of the resolved unsteady structures especially in DES simulations) of 1×10^{-5} s was maintained for the unsteady simulation. The simulations were run initially for a total of 15000 time steps (fully resolved unsteady flow was achieved by this time) to achieve fully resolved unsteady structures. Then the unsteady pressure monitors were activated and the flow simulations were run for further 15000 time steps to study the spectral contents of the pressure signals at various locations in the cavity. For analyzing the mean flow structures, the unsteady flow was averaged for 15000

time steps which corresponds to time equivalent to over 25 fundamental periods. For unsteady flow analysis, the fast Fourier transforms (FFT) were analyzed in a fft window of 8192 (i.e. all the presented fft data corresponds to the unsteady signals for 8192 time steps).

4 Geometry and Grids

Two types of 3D geometries were considered in this investigation. The first type is a three-dimensional plane cavity, which comprises a simple rectangular cutout in an otherwise infinite plate and is therefore fully described by its length-to-depth and length-to-width ratios. Hereafter the plane cavity geometry will also be referred to as the clean cavity. The second type had a store in the cavity as shown in Figure 2. The first case considered was a 12.2cm deep cavity with an L/D of 5.42 and W/D of 2.0. The second case had the same cavity dimensions as the first but it also had a store in the cavity. The third case was a 12.2cm deep cavity with an L/D of 6.25 and W/D of 2.0. The fourth case had the same dimensions as the third but it also had a store in the cavity. The last two cases were considered for two main reasons. Firstly, the L/D value in these cases is larger than the first two cases, hence, it would allow to study the flow behaviour due to increase in L/D . Secondly, the gap between the trailing edge of store and the cavity rear wall is greater in fourth case. This would allow to study the difference in the flow behaviour due to increased gap for the cavity-with-store cases. The main reason for choosing these cases was due to the availability of the experimental data. All these cavity geometries correspond to some of the many cases in the experimental investigation by Tracy and Plentovich [21]. Again, as with the geometry, the flow condition corresponds to a subset of those investigated by Tracy and Plentovich. Table 2 lists the details of all the cases investigated.

Table 1: Computed cases

Case	Depth (D)	L/D	W/D	M_∞	Store axis position	Boundary layer thickness near upstream wall (δ)
1	12.2 cm	5.42	2	0.80	N/A	1.27 cm
2	12.2 cm	5.42	2	0.80	in line with exit plane	1.27 cm
3	12.2 cm	6.25	2	0.80	N/A	1.27 cm
4	12.2 cm	6.25	2	0.80	in line with exit plane	1.27 cm

The basic design and the extent of the three-dimensional computational domain and mesh density were chosen following preliminary two-dimensional numerical simulations. Due to the excessive computational time involved in 3D unsteady computations, two-dimensional simulations were used to establish grid convergence. For this purpose three meshes were generated

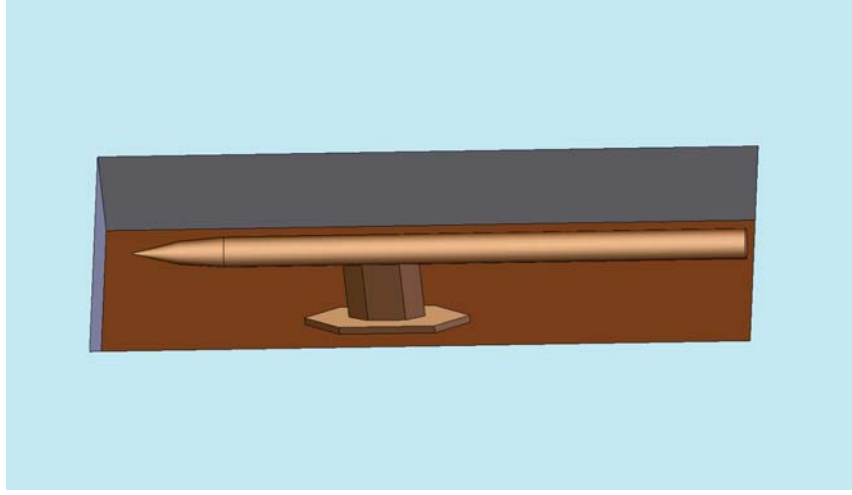


Figure 2: Isometric view of the 3D cavity with store.

with the same basic mesh topology, but with varying grid densities. In this way, an optimum 2D grid was established. The 2D grid was chosen as the basis for the 3D grid generation. For the cavity-with-store cases, The grid cell sizes inside the cavity were maintained similar to the equivalent clean cavity geometry (for the DES simulation, the 3D grid cells are ideally required to be isotropic. Hence all clean cavity meshes had near isotropic cells inside the cavity with minimum stretching. These cells sizes were used while generating the grid for the cavity-with-store cases).

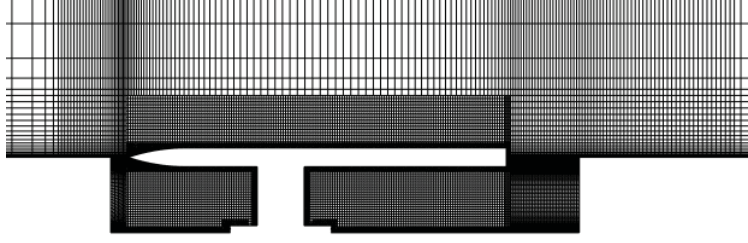
The three-dimensional computational domain extends $4L$ upstream, $5L$ downstream and $3L$ vertically and laterally from the cavity walls. The overall mesh size for all the cases was maintained approximately between 2.0 million cells to 2.75 million cells. Grid cells were clustered along all solid walls and in the region of the shear layer using a hyperbolic-tangent distribution. At the cavity leading edge, the boundary layer is resolved with approximately 20 mesh points. Figure 3 shows the section views of the grids in Cavity-with-store and empty cavity cases.

5 Results

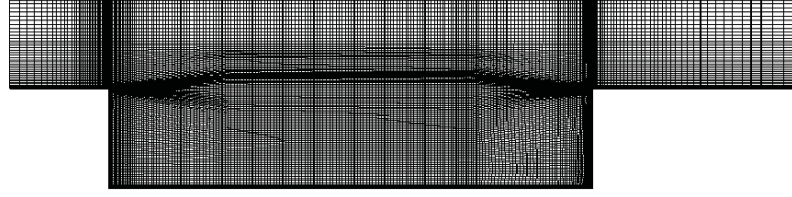
5.1 Computed Results

Cavity time-mean flow

Time-mean surface static pressure coefficient (C_p) distributions were studied to determine the mean flowfield characteristics inside the cavities. These plots are presented in Figures 4 and 5



(a) Section view of Cavity-with-store grid.



(b) grid distribution in empty cavity.

Figure 3: Structured grid distribution.

for each of the simulated cases. The mean C_p distributions for the first and the second cases are plotted in Figure 4. The flow conditions were set to match the experimental study of Stallings *et al.* [21]. The study of the mean C_p indicated that the computed C_p was initially positive for the first 17% of the cavity floor. It was negative until $x/L \approx 0.5$ with a minimum at approximately $x/L = 0.5$. The C_p then continued to rise downstream of $x/L = 0.5$, reaching a maximum value at the cavity trailing edge. This behaviour was present in both the computed cases. The influence of the presence of the store in the cavity on the static pressure distributions may be seen in terms of an increase in pressure along the cavity floor and a decrease in the maximum pressure observed along the aft wall of the cavity. In both the cases the point of maximum pressure is seen to lie at the rear end of the floor. In the experiments, however, the C_p is found to have a marginally negative value at the upstream end (first measurement was at $x/L = 0.046$) and the pressure continues to drop until approximately $x/L = 0.45$. The C_p , then, continues to rise downstream of $x/L = 0.45$, reaching a maximum value at the cavity trailing edge. From Figure 4, it can be seen that there is a negligible effect on the mean C_p due to the presence of the store in the front half of the cavity length. This is true for both computed and experimental results. The computed results over-predict the experiment by a C_p of no more than 0.025 in the front half. The rear half of the cavity shows a small effect on the C_p distribution due to the presence of the store. The computed

result slightly over-predicted the experiment but the curves have similar characteristics (i.e. similar slope). Overall the computed mean flowfield agrees reasonably well with the experiment. The small difference may be due to the influence of differences in the nature of the boundary layers at the cavity leading edge (in the computational setup and experiment) and its effect on the instability characteristics of shear layers that span the cavities. The behaviour of both the computed as well as experimental cavity floor C_p distributions suggests that the flow shares similarity with flows on the boundary between open and transitional-open types. Mean C_p plots are also compared for the the third and the fourth cases in Figure 5. Again, the flow conditions were set to emulate the experimental study of Stallings *et al.* [21]. As in the second and third cases, it can be seen that there is negligible effect on mean C_p due to the presence of the store in the front part of the cavity floor until $x/L = 0.2$ mark. Both computed and experimental data show that the C_p starts with a marginally negative value at the upstream end (first floor measurement point was at $x/L = 0.039$ in experiment). The rear half of the cavity showed only a small effect on the C_p plot due to the presence of the store. A reasonable agreement between the computed and experimental mean flowfield is evident from the comparison. The behaviour of the computed as well as experimental cavity floor C_p distributions showed that the flow shared similarity with the transitional-closed types.

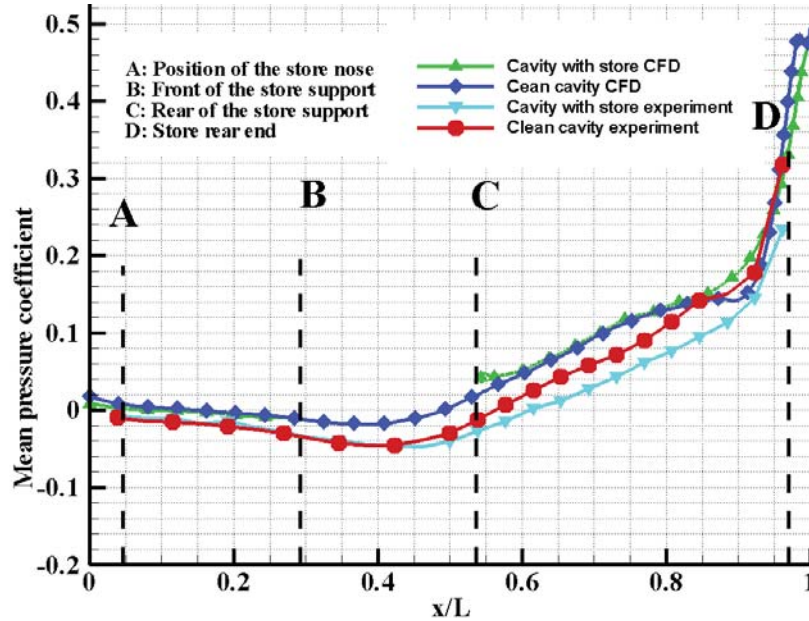


Figure 4: Mean C_p variations for clean cavity and cavity-with-store cases, $L/D = 5.42$ and $W/D = 2$.

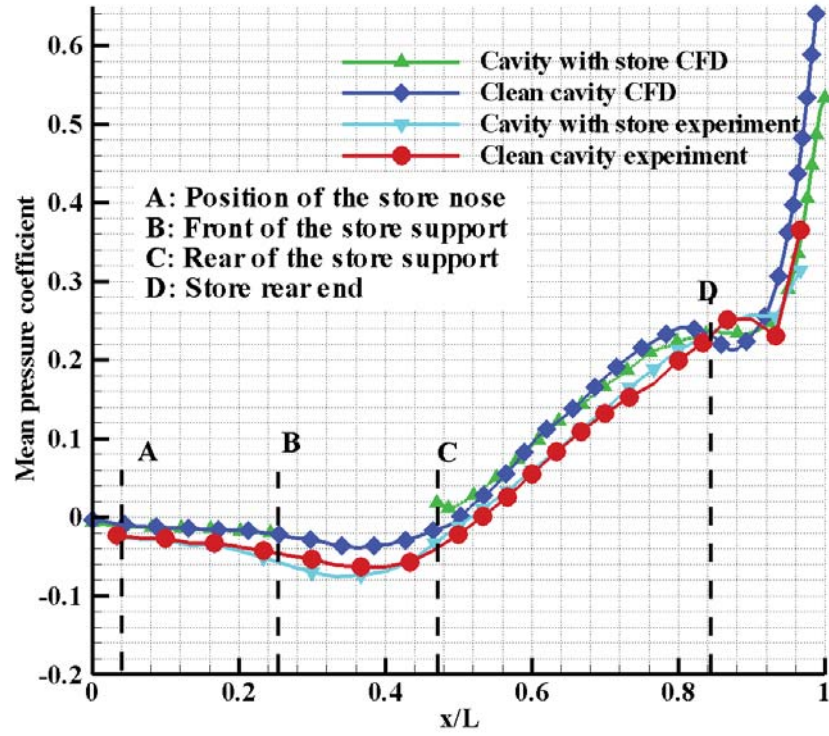


Figure 5: Mean C_p variations for clean cavity and cavity-with-store cases, $L/D = 6.25$ and $W/D = 2$.

Time-mean flow visualization

Although the mean pressure coefficient plots can be used to identify the cavity flow type and to validate against available experimental data, a more detailed study of the flow behaviour and structure inside the cavity is not possible from these plots. Hence visualization of 2D sectional streamlines using line integral convolution (LIC) images [22] along with 3D surface flow particle tracking were used to study the flow behaviour further. To study the state of the time-mean flow features inside the cavity, vortex core locations were calculated in the time-averaged CFD data and stream lines were emitted from the calculated locations. The resulting mean flow structures are presented in Figure 7 for the first case. In addition, sectional streamlines of computed time-mean velocity data are visualized using LIC in Figure 6. Figure 7 reveals the presence of two contra-rotating flow structures in the upstream third of the cavity which merge to a single, large recirculation further downstream. This is also evident from the LIC image in Figure 6(g). These structures are described in ESDU Item 02008 [12] as 'tornado-like' vortices which spiral up towards the mouth plane (i.e. the open plane) of the cavity although a description of their subsequent movement is not given. This has been further analyzed and discussed by Atvars *et al.* [23] with the aid of experiments and CFD visualization. Atvars *et al.* [23] describe that these structures are formed when the flow travelling upstream along the floor of the cavity reaches the upstream wall. The proximity of the cavity sidewall forces the flow to divert in the spanwise direction towards the centreline of the cavity. When the flow reaches the centreline plane, it meets the flow from the other side of the centreline and is forced to turn to flow downstream but is prevented from doing so by the flow travelling upstream along the cavity floor. The flow is forced to turn out towards the sidewall of the cavity which forms the vertical 'tornado-like' structures seen on the cavity floor. Our recent CFD calculations [24] showed the presence of only one 'tornado-like' vortex for a narrower cavity ($W/D = 1$). Also visible in Figure 7 are two vortices trailing downstream from the downstream corners of the cavity which is consistent with the flow visualisation works of Taborda *et al.* [25]. The LIC images of sectional streamlines at various spanwise locations (i.e. Figures 6[a-e]) also clearly indicate the three-dimensionality in the time-mean flow inside the cavity. Both the variation in the position of the core of the recirculating structure across the span of the cavity and the appearance of a secondary recirculating region upstream of the main recirculation is evident for all spanwise locations except $z/W = 0.4$ and $z/W = 0.5$.

Time-mean flowfields were also visualised for the second case (i.e. cavity-with-store case) to

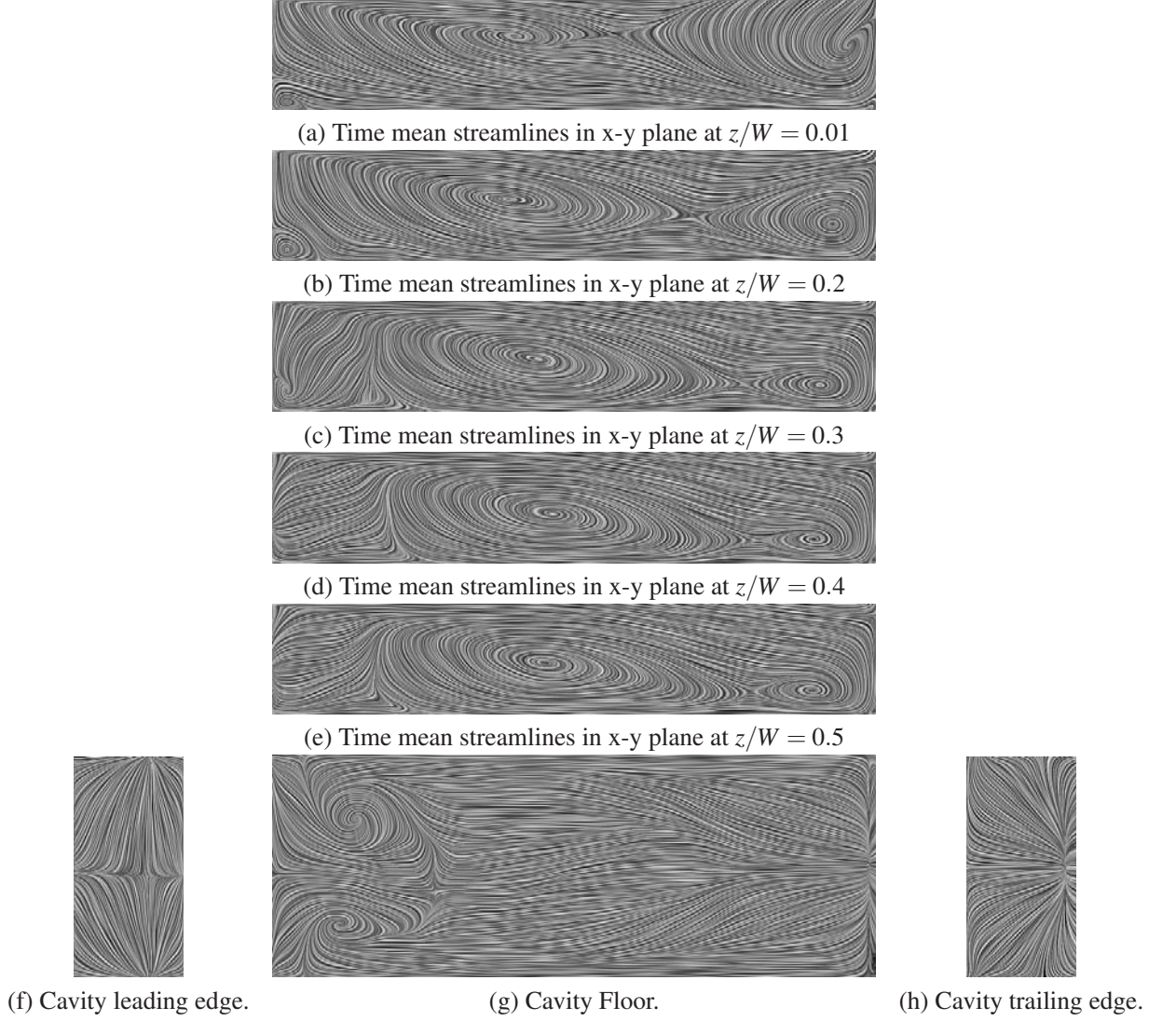


Figure 6: Mean flow map in cavity using Line Integral Convolution, $L/D = 5.42$, $W/D = 2$ and $M_\infty = 0.80$.

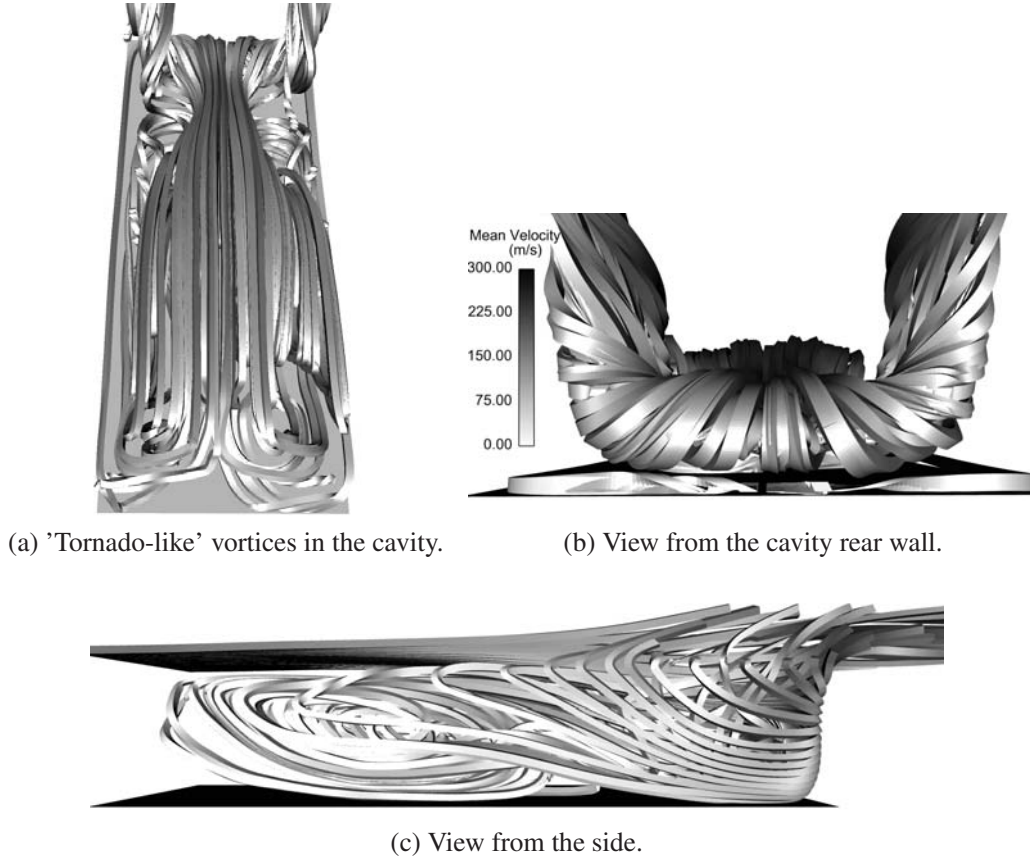


Figure 7: Time-mean streamlines for 3D cavity, $L/D = 5.42$, $W/D = 2$ and $M_\infty = 0.80$.

understand the time development of the mean flow due to the presence of the store. Figures 8 and 9 show the state of the mean flow features for this case. Most of the global flow features observed in the first case are seen to exist in this case. However, some noticeable differences can also be seen after careful study of the images. Although, Figure 9 and the LIC image in Figure 8(j) hint towards the presence of two recirculating structures on either side of supporting strut upstream of the cavity, these structures are very weak in comparison to the structures seen in Figures 7 and 6(g). However, the presence of two strong 'tornado-like' structures are clearly evident in Figure 8(g) which is a section view at half the cavity depth. This can be further clarified with the aid of description on formation of these structures by Atvars *et al.* [23]. When the flow travelling upstream along the floor reaches the upstream wall of the cavity the proximity of the cavity sidewall forces it to divert in the spanwise direction towards the centreline. On reaching the centreline plane, it meets the flow from the other side of the centreline and is forced to turn to flow downstream. Unlike in the clean cavity case, the flow travelling upstream along the cavity floor encounters the flat base of the supporting strut. Hence the downstream travelling flow is able to travel without forming a complete recirculation. At a plane parallel to the floor above the support base, however, the strut cross section is smaller and is more slender. This allows the flow travelling upstream to continue to a large extent, thereby forcing the downstream travelling flow to turn in a vertical spiral. This explains the reappearance of the 'tornado-like' structures in Figure 8(g). Also the variation in the position of the core of the recirculating structure across the span of the cavity is less noticeable from the LIC images in Figure 8. This indicates that the spanwise flow structure off the centre plane shows smaller 3D effects compared to the clean cavity case (i.e. the first case). However, a secondary recirculating region in the upstream of the main recirculation is found to exist at various spanwise locations except $z/W = 0.4$ and $z/W = 0.5$ consistent with the previous observations (in the first case). The upstream view of the cavity trailing edge in Figure 9 reveals that the streamlines are seen to have divided due to the presence of the store and the supporting strut. The upstream view from the rear of the cavity [see Figure 9(b)] clearly shows the streamlines rolling up in two halves on either side of the store body.

Figures 10 and 11 show the time-mean flowfield for the third and the fourth cases. These images also reaffirm most of the global flow features observed in the first and the second cases. As in the first case, Figures 11(a) and the LIC image in Figure 10(e) reveal the presence of two 'tornado-like' structures in the upstream third of the cavity which merge to a single, large recir-

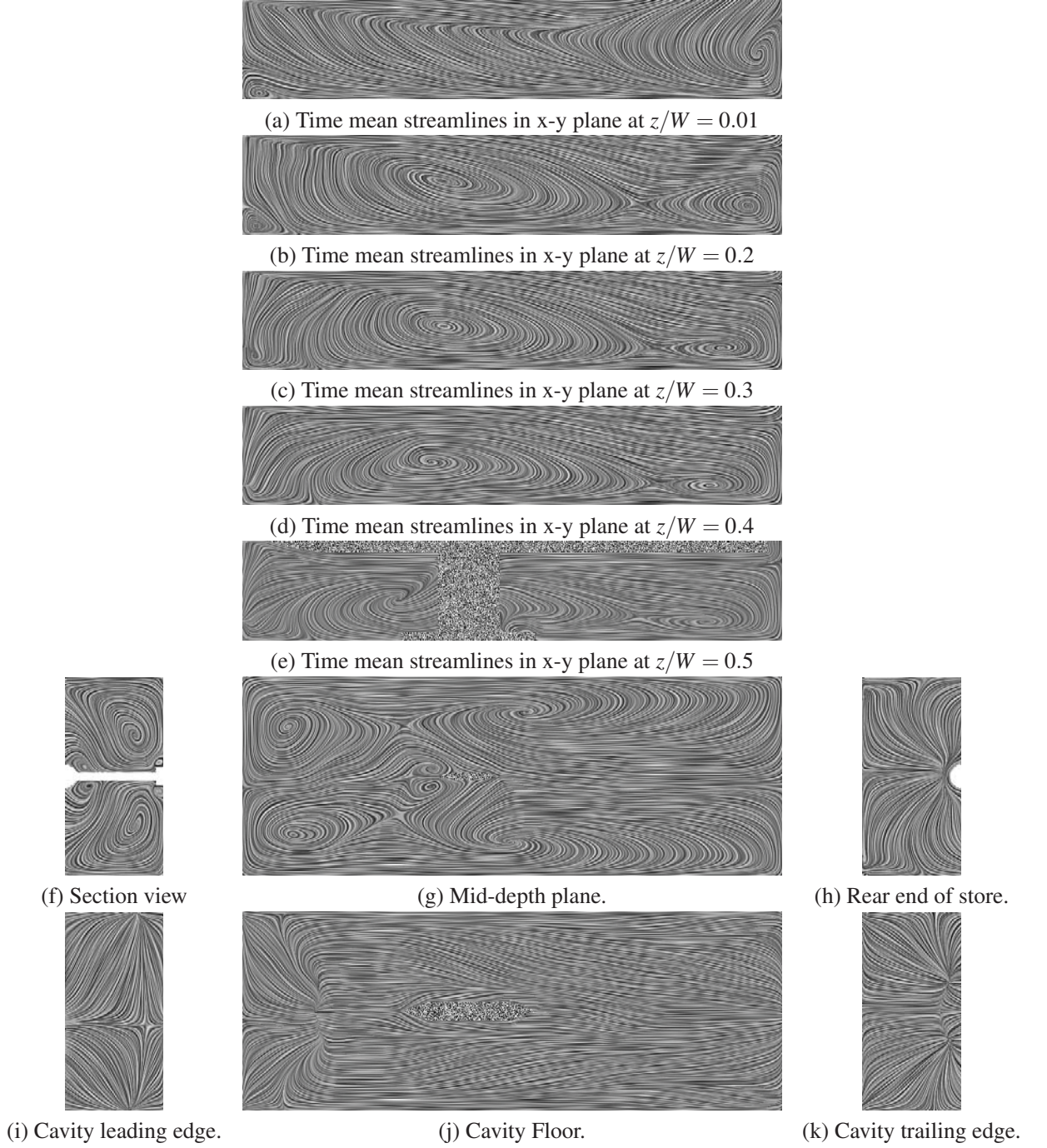
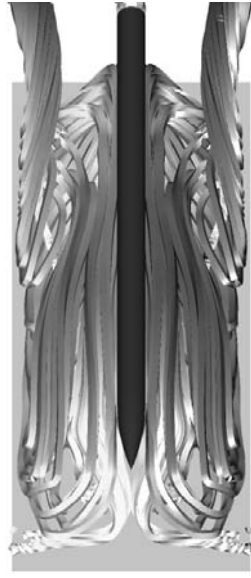


Figure 8: Mean flow surface maps in cavity with store using Line Integral Convolution, $L/D = 5.42$, $W/D = 2$ and $M_\infty = 0.80$.

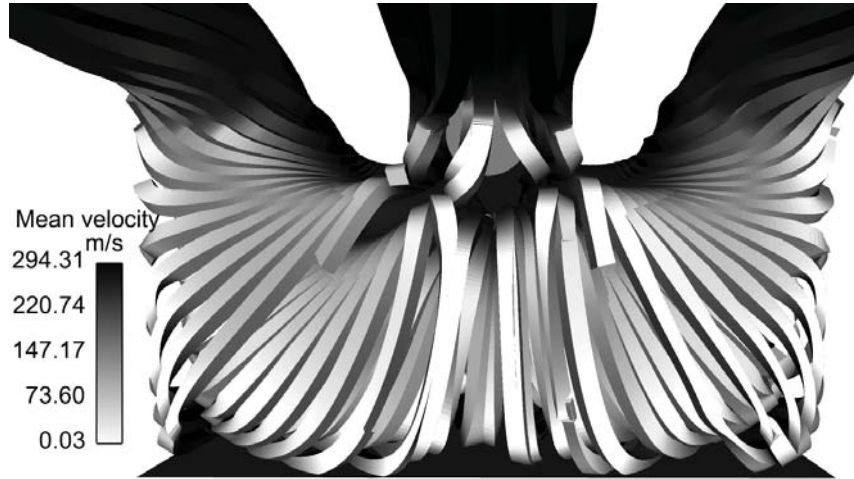


(a) Flow structure in the cavity.

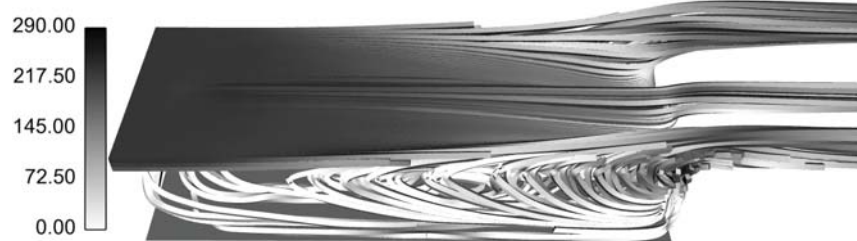


(b) View from the cavity rear wall.

Streamlines released from vortex cores inside the cavity.



(c) View from the cavity rear wall.



(d) View from the side.

Figure 9: Time-mean streamlines for 3D cavity with store, $L/D = 5.42$, $W/D = 2$ and $M_\infty = 0.80$.

ulation further downstream. A third recirculating region is found to exist in the downstream end of the main recirculating region for this case from Figure 10. The LIC images at various spanwise locations (i.e. Figures 10[a-c]) also reveal the three-dimensionality in the time-mean flow inside the cavity. The fourth case (cavity with store) also revealed similar mean flow features which were observed in the second case. As in the second case, the upstream view of cavity trailing edge in Figure 11(d) reveals that the streamlines are seen to have divided due to the presence of the store and the supporting strut. The effect of the increased gap on the flowfield is found to be negligible.

Time-dependent flowfield

Unsteady computations were performed for all the cavity cases. The unsteady flowfield shows the presence of a warping of the vortex axis across the span of the cavity. This occurs due to the result of the end walls retarding the growth of the vortical structures as they move downstream of the cavity. Figures 12 and 13 show the iso-surfaces of the vorticity magnitude for the clean cavity and the cavity with the store respectively. From the figures, the vorticity iso-surface can be seen to undergo warping in two parts due to the presence of the store (i.e. the store is seen to act as a central wall which promotes warping of the vortices on both halves). As the vortical structures in these regions reach the trailing edge, the vortex axis is aligned with the streamwise direction. Then the 3D flow in the end wall regions leads to the formation of the streamwise vortices which is also clear from the study of time-mean streamlines in Figure 9(c).

To study the unsteady flow quantitatively, the frequency content of the nearfield pressure fluctuations was extracted using fast Fourier transforms. Figures 14 and 15 show the frequency content of the pressure signals for the first and the second cases. Figure 16 compares the pressure spectra from the two cases at two different positions along the cavity centreline.

Predicted mode frequencies from the two cases along with the calculation using the modified Rossiter formula are presented in Table 2. From the results, the first mode frequency from the clean cavity case is found to agree well with the modified Rossiter formula. The dominant mode, however, is not the first mode and the dominant peak occurs at 212 Hz. This frequency is significantly lower compared to the second mode of 279 Hz predicted by the modified Rossiter formula. Higher order modes are absent in the computed spectra. The cavity-with-store case, however, has many peaks in the pressure spectra and the corresponding mode frequencies agree well with the Rossiter formula. Up to five Rossiter modes are clearly present for the store case

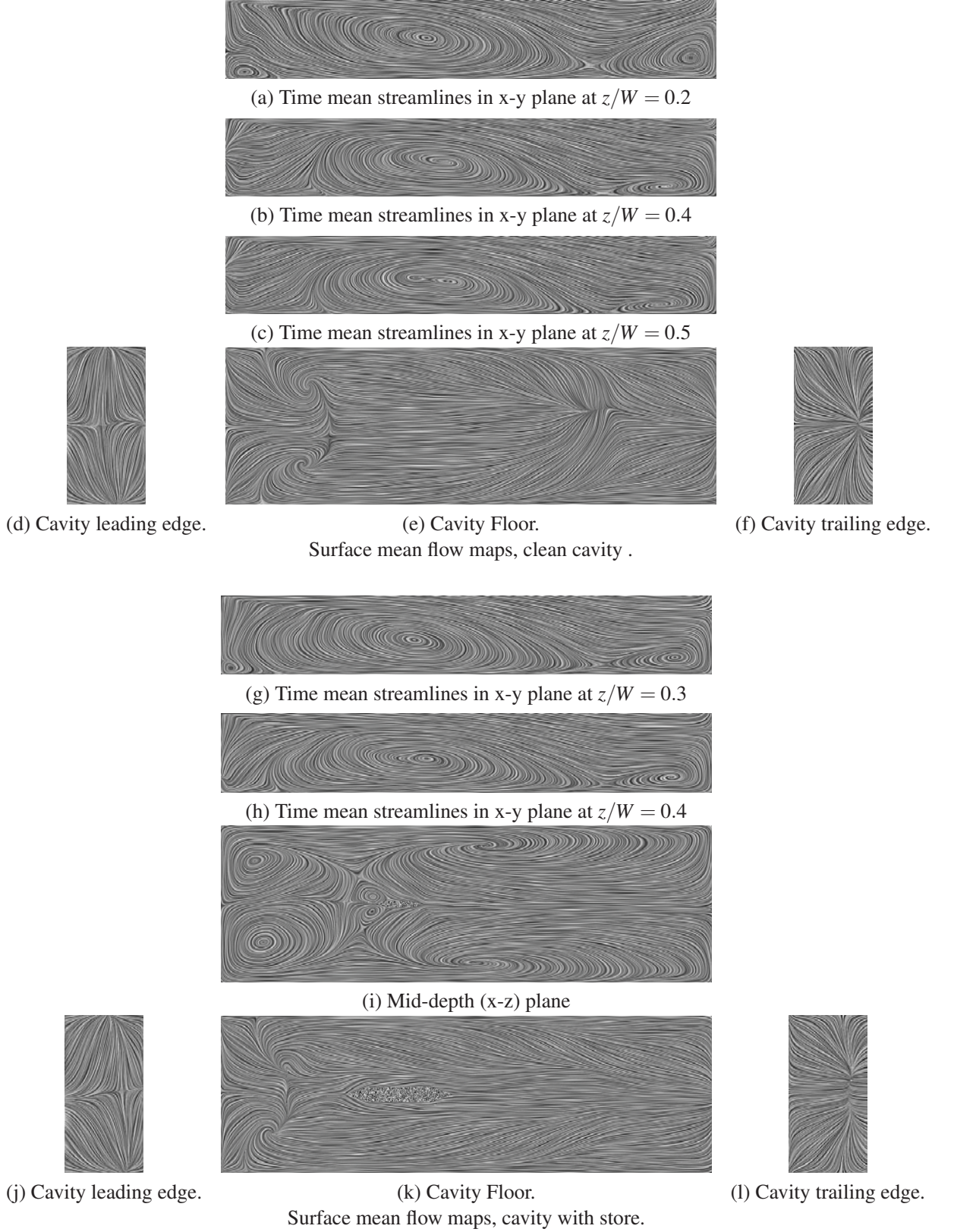
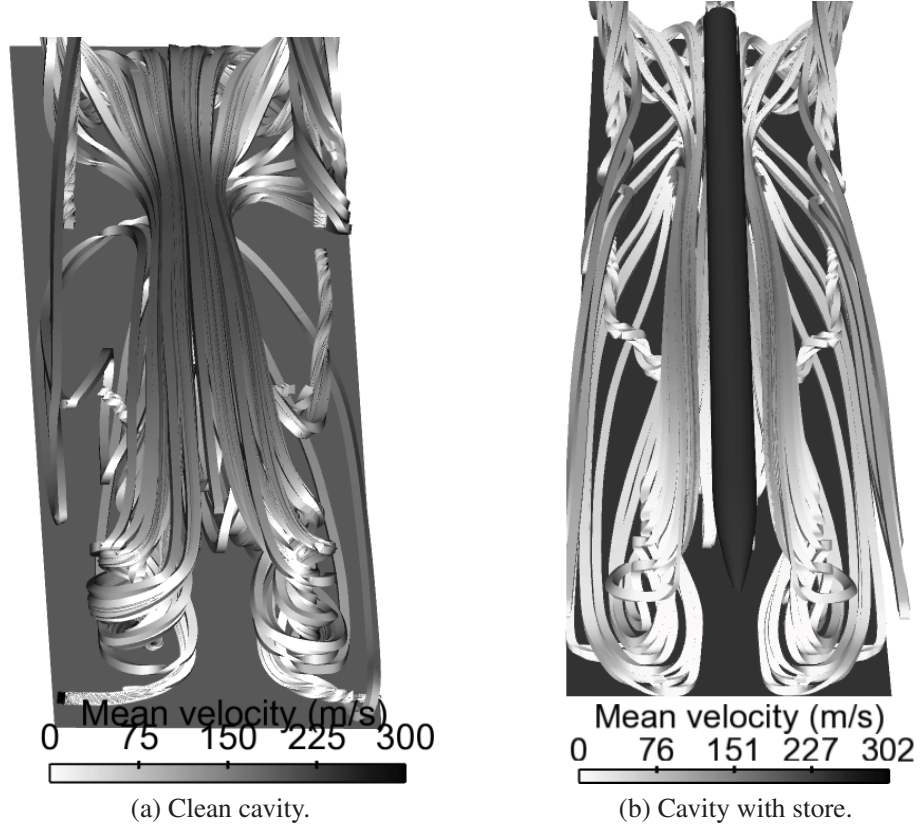
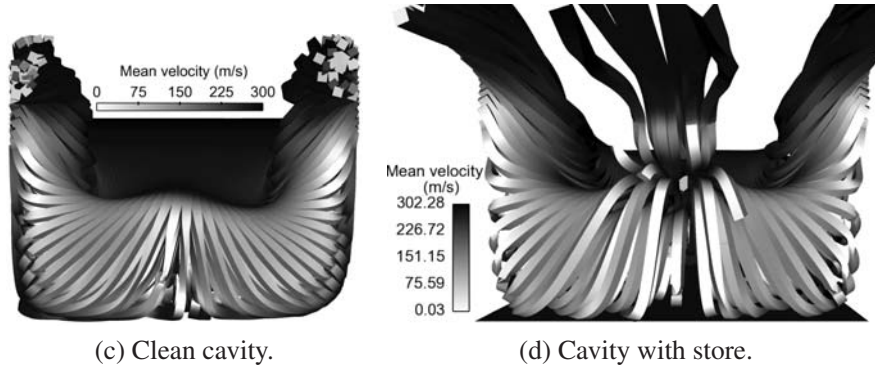


Figure 10: Mean flow maps using Line Integral Convolution, $L/D = 6.25$, $W/D = 2$ and $M_\infty = 0.80$.



Streamlines released from vortex cores inside the cavity.



View from the cavity rear wall.

Figure 11: Time-mean streamlines, $L/D = 6.25$, $W/D = 2$ and $M_\infty = 0.80$.

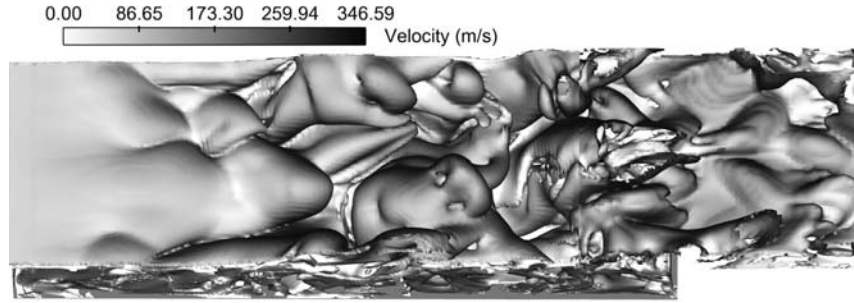


Figure 12: Vorticity iso-surface, view from the top of 3D clean cavity, $L/D = 6.25$ and $W/D = 2$.

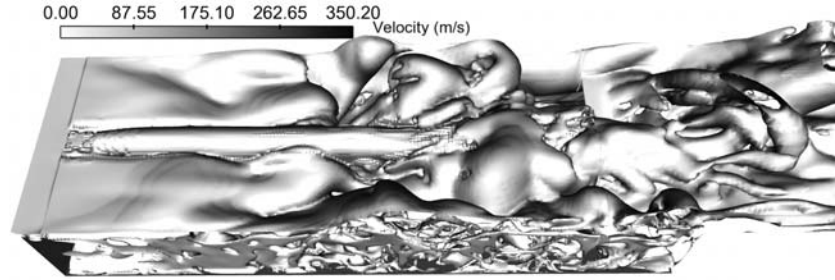
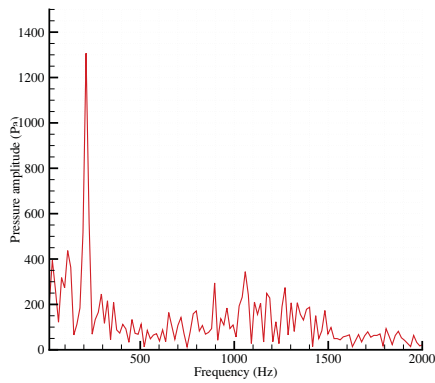
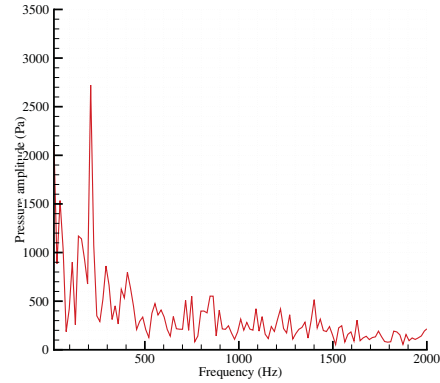


Figure 13: Vorticity iso-surface, view from the top of 3D cavity with a store, $L/D = 6.25$ and $W/D = 2$.



(a) Floor at $x/L=0.10$.



(b) Floor at $x/L=0.90$.

Figure 14: Clean cavity pressure spectra at floor, $L/D = 5.42$ and $W/D = 2$.

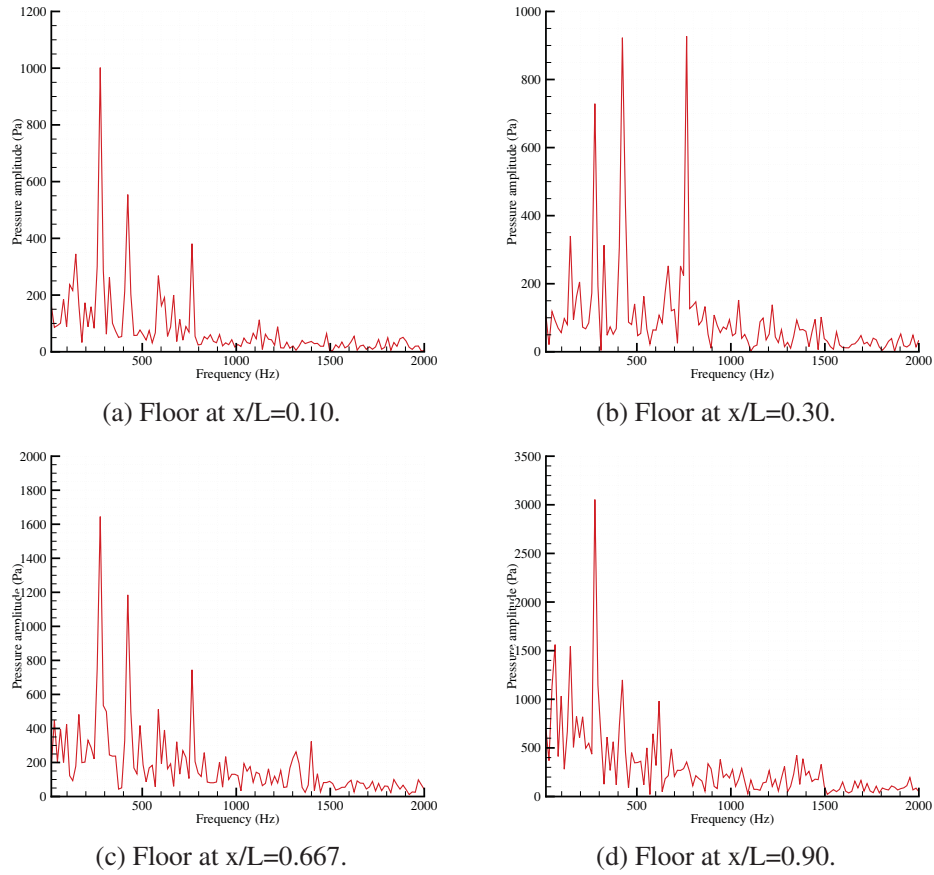


Figure 15: Cavity with store pressure spectra at floor, $L/D = 5.42$ and $W/D = 2$.

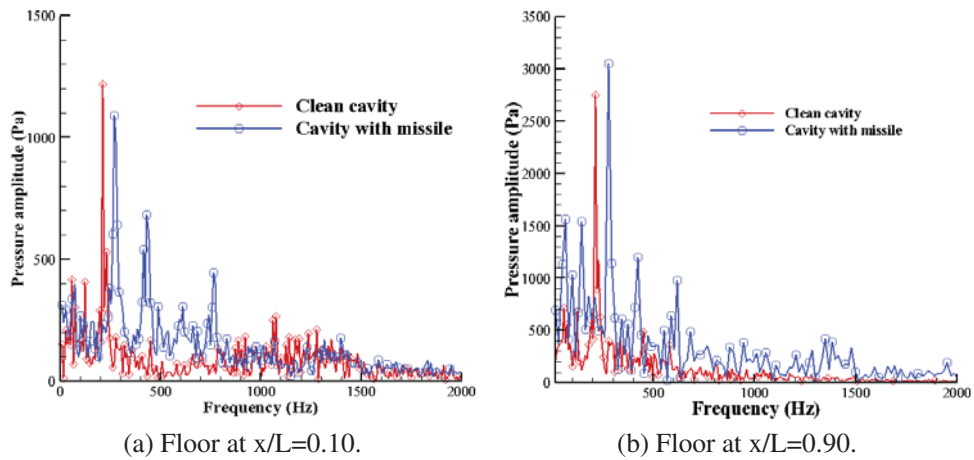


Figure 16: Floor centreline pressure spectra comparison for clean cavity and cavity with store, $L/D = 5.42$ and $W/D = 2$.

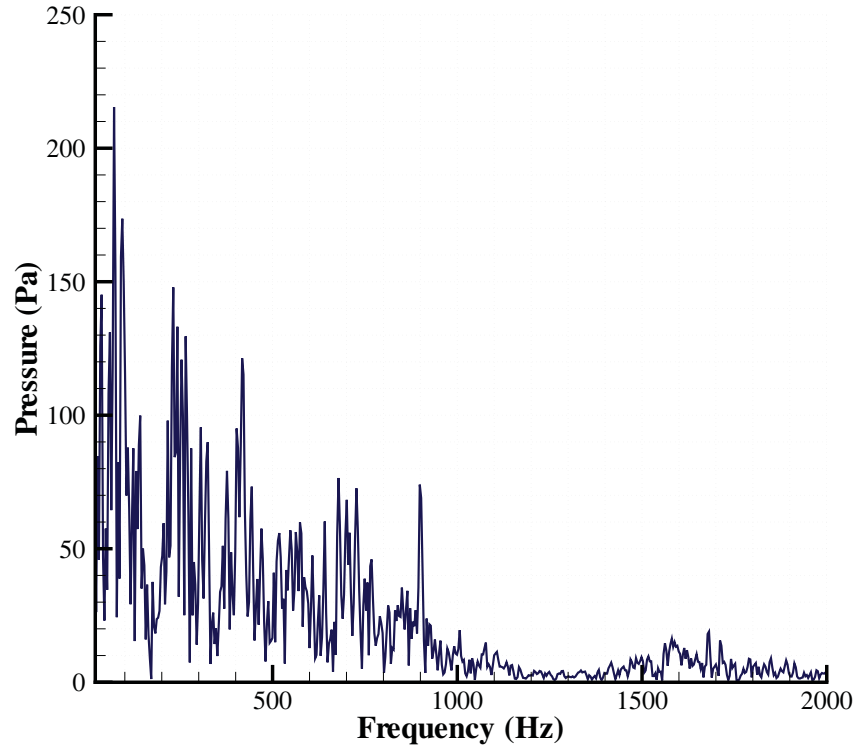
in contrast to the clean cavity which only had the first and second modes present. High speed cavity flows are characterised by the existence of more than a single dominant mode and these multi-modes are found to couple non-linearly resulting in amplitude modulations at different frequencies. This is most probable for the clean cavity because spanwise flow fluctuations (i.e. in the z -axis direction) are dominant compared to the store case which has less pronounced spanwise flow. Hence a coupling between the lateral and longitudinal instabilities may have resulted in a dominant peak at 212 Hz for the clean cavity case. In the case of cavity-with-store, however, the spanwise flow is less pronounced i.e. the flowfield on either side of the store behaves close to 2D flow. Also the mode frequency prediction by the Rossiter formula is based on the 2D cavity. This is thought to be the reason for better agreement of cavity-with-store case mode frequencies with theory.

Table 2: Comparison of mode frequencies (Hz) for cavity with L/D ratio of 5.42

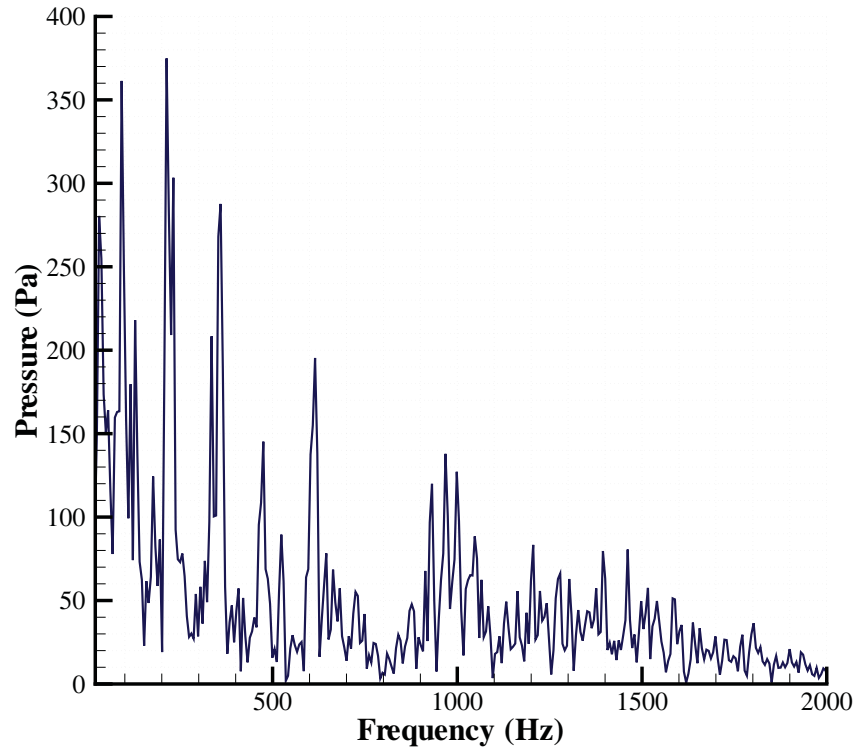
mode	Clean cavity	Cavity with store	Modified Rossiter Formula
1	114	145	111.4
2	212	276.6	279
3	–	424	445
4	–	618	615
5	–	765	782

The last two cavity cases studied had a L/D ratio of 6.25 and W/D ratio of 2. Again, one of the two was an empty cavity whereas the other had a store with a supporting strut. Figure 17 shows the frequency content of the pressure signals for these last two cases at one point on the cavity centreline, near the upstream wall. Predicted mode frequencies from the two cases are presented in Table 3. As in the previous two cases, the first mode frequency from the clean cavity case (the third case) is found to agree well with modified Rossiter formula. However, the first mode is not the dominant mode and the dominant peak occurs at 268 Hz. This frequency is different to the second mode of 234 Hz predicted by the modified Rossiter formula. The cavity-with-store case, however, has many peaks in the pressure spectra (consistent with the observations in the second case) and the corresponding mode frequencies agree reasonably well with the Rossiter formula. Up to five Rossiter modes are clearly present for the store case in contrast to the clean cavity which only had the first and second modes present. These observations are consistent with the results from the first and the second cases.

The mean flowfield visualisation in the time-mean flow study clearly indicated that the flowfield was divided in two halves with little evidence of flow across the store and supporting strut.



(a) Clean cavity.



(b) Cavity with store.

Figure 17: Floor centreline pressure spectra at $x/L=0.10$, $L/D = 6.25$ and $W/D = 2$.

Table 3: Comparison of mode frequencies (Hz) for cavity with L/D ratio of 6.25

mode	Clean cavity	Cavity with store	Modified Rossiter Formula
1	97	91.7	89
2	268	214.0	234
3	–	360.7	380
4	–	477.0	525
5	–	617.0	670

This blockage effect of store and strut on the spanwise flow might have reduced the possibility of spanwise and streamwise flow fluctuations undergoing non-linear coupling to result in amplitude modulations. Computed results indicate that the presence of the store acts as a breaker to the spanwise flow fluctuations and is thought to be the reason for the co-existence of multiple modes without the coupling among them.

6 Conclusion

The time-mean flowfield was studied computationally for two different rectangular cavities in transonic speed. Mean pressure coefficients were compared for both clean cavity and cavity-with-store cases against experimental data and the results showed reasonably good agreement between the two. The clean cavity and the cavity-with-store case have negligible differences in their C_p distribution over the front half of the cavity whereas the difference was more pronounced at the rear half. The presence of a store is seen to limit the spanwise flow in the cavity and this is thought to have caused this difference. A small difference is found to exist between the experimental and the computational results. This difference may be due to the lack of sufficient experimental details on various parameters that affect the cavity flowfield e.g. incoming boundary layer thickness (δ), tunnel turbulence levels etc.

For the first case, the first mode frequency is found to agree well with the modified Rossiter formula. The dominant mode, however, is not the first mode and the dominant peak occurs at 212 Hz. This frequency is significantly lower compared to the second mode of 279 Hz predicted by the modified Rossiter formula. Higher order modes are absent in the computed spectra. In the case of high speed cavity flows, the existence of more than a single dominant mode is likely and these multi-modes tend to couple non-linearly resulting in low frequency modulation of the Rossiter modes. This is thought to be the main reason for the presence of the dominant mode at 212 Hz.

A study of the computed unsteady pressure spectra for the second case found the presence of many peaks and the corresponding mode frequencies are found to agree reasonably well with the Rossiter modes. Up to five Rossiter modes were found to be present for this case, in contrast to the clean cavity case. The mean flowfield visualisation in the time-mean flow study clearly showed that the flowfield was divided in two halves with little evidence of flow across the missile and supporting strut. This blockage effect of missile and strut on the spanwise flow might have reduced the interaction of spanwise and streamwise flow fluctuations undergoing non-linear coupling to result in amplitude modulations. This may be the reason for the co-existence of multiple modes without the coupling among them.

Study of the unsteady pressure spectra for the third and the fourth cases reaffirms most of the unsteady behaviour observed in the first and the second cases. For the third case, computed result reveals the presence of two modes and only the first mode frequency is found to agree well with the modified Rossiter formula. The dominant mode, which is not the first mode, has its peak at 268 Hz. This frequency is different to the second mode of 234 Hz predicted by the modified Rossiter formula. Higher order modes are absent in the computed spectra. These observations are consistent with the results of the first case. As in the second case, many peaks are present in the fourth case (cavity-with-store case) and the corresponding mode frequencies also agree well with the Rossiter modes. The blockage effect of store and strut on the spanwise flow is thought to be the reason which limits the interaction of spanwise and streamwise flow fluctuations undergoing non-linear coupling to result in amplitude modulations. The mean flowfield visualisation in the time-mean flow study also clearly showed that the flowfield was divided in two halves with little evidence of spanwise flow across the missile and supporting strut. Further studies are ongoing to understand this flow behaviour better.

References

- [1] Dix, R. E. and Bauer, R. C., "Experimental and predicted acoustic amplitudes in a rectangular cavity," No. AIAA-2002-0472, 2000.
- [2] Srinivisan, S. and Baysal, O., "Navier-Stokes calculations of transonic flow past cavities," *Journal of Fluid Engineering*, Vol. 113, September 1991, pp. 369-376.
- [3] Tam, C. K. W. and Block, P. J. W., "On the tones and pressure oscillations induced by flow over rectangular cavities," *Journal of Fluid Mechanics*, Vol. 89, 1978, pp. 373-399.

- [4] Stallings, R. and Wilcox, F., "Experimental cavity pressure distributions at supersonic speeds," Tech. Rep. NASA-TP-2683, NASA, June 1987.
- [5] Xiao, X., Edwards, J. R., and Hassan, H. A., "Blending Functions in Hybrid Large-Eddy/Reynolds-Averaged Navier-Stokes Simulations," *AIAA Journal*, Vol. 42, No. 12, 2004, pp. 2508–2515.
- [6] Spalart, P. R. and Allmaras, S. R., "Comments on the feasibility of LES for wings and on a hybrid RANS/LES approach," Proceedings of first AFOSR international conference on DNS/LES, Ruston, Louisiana, USA, August 1997.
- [7] Nichols, R. H., "Comparison of Hybrid Turbulence Models for a Circular Cylinder and a Cavity," *AIAA Journal*, Vol. 46, No. 6, 2006, pp. 1207–1219.
- [8] Sinha, N., Dash, S., Chidambaram, N., and Findlay, D., "A Perspective on the Simulation of Cavity Aeroacoustics," No. AIAA-1998-0286, Jan. 1998.
- [9] Spalart, P. R., Deck, S., Shur, M. L., Squires, K. D., Strelets, M. K., and Travin, A., "A new version of detached-eddy simulation, resistant to ambiguous grid densities," *Theoretical and Computational Fluid Dynamics*, Vol. 20, 2006, pp. 181–195.
- [10] Charwat, A. F., Roos, J. N., Dewey, F. C., and Hitz, J. A., "An Investigation of Separated Flows Part 1 : The Pressure Field," *Journal of Aerospace Sciences*, Vol. 28, No. 6, 1961, pp. 457–470.
- [11] Charwat, A. F., Roos, J. N., Dewey, F. C., and Hitz, J. A., "An Investigation of Separated Flows Part 2 : Flow in the Cavity and Heat Transfer," *Journal of Aerospace Sciences*, Vol. 28, No. 7, 1961, pp. 513–527.
- [12] ESDU, *Aerodynamics and aero-acoustics of rectangular planform cavities. Part I: Time-averaged flow*, IHS ESDU, London, UK, 2004, ESDU Data Item 02008.
- [13] Plentovich, E., "Three-dimensional cavity flow fields at subsonic and transonic speeds," Tech. Rep. NASA-TM-4209, NASA Langley Research Center, 1992.
- [14] Tracy, M. B. and Plentovich, E., "Measurements of fluctuating pressure in a rectangular cavity in transonic flow at high Reynolds number," Tech. Rep. NASA-TM-4363, NASA Langley Research Center, 1992.

- [15] Rossiter, J., “Wind-tunnel experiments on the flow over rectangular cavities at subsonic and transonic speeds,” Tech. Rep. 3438, Aeronautical Research Council Reports and Memoranda, 1966.
- [16] Heller, H., Holmes, D., and Covert, E., “Flow-induced pressure oscillations in shallow cavities,” *Journal of Sound and Vibration*, Vol. 18, 1971, pp. 545–553.
- [17] Khanal, B., Knowles, K., and Saddington, A., “Computational Study of Cavity Flowfield at Transonic Speeds,” No. AIAA–2009–701, 47th AIAA Aerospace Sciences Meeting, Orlando, Florida, 2009.
- [18] Kim, S., Dai, Y., Koutsavdis, E. K., Sovani, S., Kadam, N. A., and Ravuri, K. M. R., “A Versatile Implementation of Acoustic Analogy Based Noise Prediction Method in a General-Purpose CFD Code,” No. AIAA–2003–3202, 9th AIAA/CEAS Aeroacoustics Conference and Exhibit, Hilton Head, South Carolina, USA, May 2003.
- [19] Mathey, F., Morin, O., Caruelle, B., and Debatin, K., “Simulation of aeroacoustic sources in aircraft climate control systems,” No. AIAA–2006–2493, 12th AIAA/CEAS Aeroacoustics Conference and Exhibit, Cambridge, Massachusetts, USA, May 2006.
- [20] Spalart, P. R. and Allmaras, S. R., “A one-equation turbulence model for aerodynamic flows,” No. AIAA–1992–0439, 30th AIAA Aerospace Sciences Meeting and Exhibit, Reno, Nevada, USA, January 1992.
- [21] Stallings, R. L., Plentovich, E. B., Tracey, M. B., and Hemsch, M. J., “Measurements of store forces and moments and cavity pressures for a generic store in and near a box cavity at subsonic and transonic speeds,” Tech. Rep. NASA–TM–4611, NASA, May 2002.
- [22] Knowles, R. D., Finnis, M. V., Saddington, A. J., and Knowles, K., “Planar visualization of vortical flows,” *Proceedings of IMechE Part G: Journal of Aerospace Engineering*, Vol. 220, No. G6, 2006, pp. 619–627, Special Issue on Integrating CFD and Experiments in Aerodynamics.
- [23] Atvars, K., Knowles, K., Ritchie, S. A., and Lawson, N. J., “Experimental and computational investigation of an ‘open’ transonic cavity flow,” *Proceedings of the Institution of Mechanical Engineers, Part G: Journal of Aerospace Engineering*, Vol. 23, No. 4, 2009, pp. 357–368.

- [24] Khanal, B., Knowles, K., and Saddington, A. J., "Study of cavity unsteady flowfield," No. ISSN0377-8312, 4th Symposium on Integrating CFD and Experiments in Aerodynamics, Belgium, 2009.
- [25] Taborda, N. M., Bray, D., and Knowles, K., "Visualisation of three-dimensional cavity flows," No. ExHFT5, In 5th World Conference on Experimental Heat Transfer, Fluid Mechanics and Thermodynamics, Thessaloniki, Greece, 2001.

Computational investigation of cavity flow control using a passive device

Khanal, Bidur

2012-12-31T00:00:00Z

Khanal B, Knowles K, Saddington AJ. (2012) Computational investigation of cavity flow control using a passive device. The Aeronautical Journal, Volume 116 , Issue 1176, February 2012, pp. 153-174
<http://dspace.lib.cranfield.ac.uk/handle/1826/8083>

Downloaded from CERES Research Repository, Cranfield University